

Influence of lateral heterogeneities on strike-slip faults behavior: Insights from analogue models.

Sandra González-Muñoz¹, Guido Schreurs², Timothy C. Schmid², Fidel Martín-
González¹

¹Área de Geología - ESCET, TECVOLRISK Research Group, Universidad Rey Juan Carlos. C/Tulipan
s/n, Mostoles, 28933 Madrid, Spain

² Institute of Geological Sciences, University of Bern, Bern, Switzerland

Correspondence to: Sandra González Muñoz (sandra.gonzalezmu@urjc.es)

Abstract

This study investigates how lithological changes can affect the strike-slip faults propagation patterns using analogue models. Strike-slip fault zones are long structures that may cut across pre-existing tectonic or lithological steep boundaries. How strike-slip faulting is affected by a laterally heterogeneous upper crust is crucial for understanding the evolution of regional and local fault patterns, stress reorientations, and seismic hazard. Our models undergo sinistral distributed strike-slip shear (simple shear) and have been analyzed by Particle Image Velocimetry (PIV). We use quartz sand and microbeads as brittle analogue materials over a viscous mixture to distribute the deformation through the model. The first models investigate strike-slip faulting in a homogeneous upper crust by using quartz sand or microbeads only. Three further models examine how the presence of a central section which laterally differs in its properties, influences strike-slip faulting. The main observations are the following:

- The homogeneous upper crust shows typical Mohr-Coulomb strike-slip faults, with synthetic fault strikes related to the angle of internal friction of the material used
- The heterogeneity upper crust has a profound effect on synthetic fault propagation, interaction and linkage as well as the kinematic evolution of antithetic faults that rotate around a vertical axis.
- The orientation of the central section determines whether antithetic fault activity concentrates along the entire length of the central contact or not. In the first case, fault activity is segmented or the number of different faults formed is increased in distinct domains. In the second case, the

28 properties of the central material determines fault propagation, interaction and/or linkage across
29 the central domain.

- 30 • These findings have potential implications for nature have been seen in the NW Iberian Peninsula.
31 In this area the change of direction of the sinistral faults and the position of the antithetic faults
32 can be explained due to lithological change.

33 **Keywords**

34 Strike-slip fault zone, Fault interaction, Fault linkage, Mechanical strength contrast, Analogue modelling

35

36 **1. Introduction**

37 Strike-slip fault systems in nature extend from a few meters to several hundred kilometers and typically
38 have complex geometries consisting of separate fault segments offset from each other or comprising
39 anastomosing, linked faults (e.g., Aydin and Nur, 1982; Barka and Kadinsky-Cade, 1988; Wesnousky,
40 1988; Stirling et al., 1996; Kim et al., 2004). The evolution of strike-slip fault systems has been studied
41 in numerous studies focused on the process of offset formation and therefore, basin development,
42 change of fault polarity and parameters controlling segmentation (e.g., Riedel, 1929; Anderson, 1951;
43 Deng et al., 1986; Sylvester, 1988; Dooley and Schreurs, 2012; Hatem et al., 2017; Lefevre et al.,
44 2020a; Visage et al., 2023). Understanding strike-slip fault interaction and linkage is important for its
45 implications on seismic hazard (Petersen et al., 2011; Bullock et al., 2014), in terms of dynamics, fault
46 growth and size of earthquakes (e.g. Aki, 1989; Harris and Day, 1999; Scholz, 2002; Wesnousky, 2006;
47 Shaw and Dieterich, 2007; de Jossineau and Aydin, 2009; Preuss et al., 2019); but also in terms of
48 regional stress orientations (Kirkland et al., 2008) and in view of the location of geothermal and
49 hydrocarbon resources (e.g. Sibson, 1985; Martel and Peterson, 1991; Aydin, 2000; Odling et al.,
50 2004; Cazarin et al., 2021).

51 How faults interact or link is considered to be a function of loading, stress disturbances, rheology and
52 the geometry of pre-existing structures (e.g., Kim et al., 2004; Myers and Aydin, 2004; Peacock and
53 Sanderson, 1991, 1992; Burgmann and Pollard, 1994; Sibson, 1985; Gamond, 1983; Rispoli, 1981;
54 Wesnousky, 1988). Various studies have investigated the influence of vertical changes in upper crustal
55 strength (e.g. a horizontal sedimentary sequence comprising layers or bodies of different strengths) on

56 strike-slip fault orientation, segmentation, linkage, and displacement. These studies used field
57 observations, combined with analytical and numerical methods (e.g. Du and Aydin, 1995; Aydin and
58 Berryman, 2010; De Dontney et al., 2011), or analogue models (Richard, 1991; Richard et al., 1995;
59 Gomes et al., 2019; Gabrielsen et al., 2023; Venancio and Alves Da Silva, 2023). However, it is also
60 important to consider the evolution of strike-slip fault systems in a laterally heterogeneous upper crust.
61 Strike-slip faults often extend laterally over considerable distances and are thus expected to be
62 influenced by steeply oriented pre-existing tectonic or lithological boundaries having rocks with
63 contrasting strength on either side. Such (sub)vertical contacts often occur at terrane boundaries or
64 within crustal blocks comprising rock units with contrasting strengths, e.g. a magmatic body with steep
65 margins that intruded into a sedimentary sequence. To our knowledge no modelling studies have yet
66 investigated how strike-slip fault systems are affected by steeply dipping contacts separating different
67 rock types. Here we use scaled analogue model experiments analysed by Particle Imaging Velocimetry
68 (PIV) to assess the role of vertically oriented domains of contrasting brittle strength in the upper crust
69 on fault kinematics in distributed strike-slip shear. The models were inspired by the deformation pattern
70 of the NW Iberian Peninsula, which has undergone sinistral shearing during the Alpine Orogeny (e.g.
71 Martínez Catalán, 2011; Vergés et al., 2019). This particular area shows a system of sinistral faults that
72 cross lithological domains with contrasting properties and part of their segmentation is conditioned by
73 these domains.

74 75 **2. Methods**

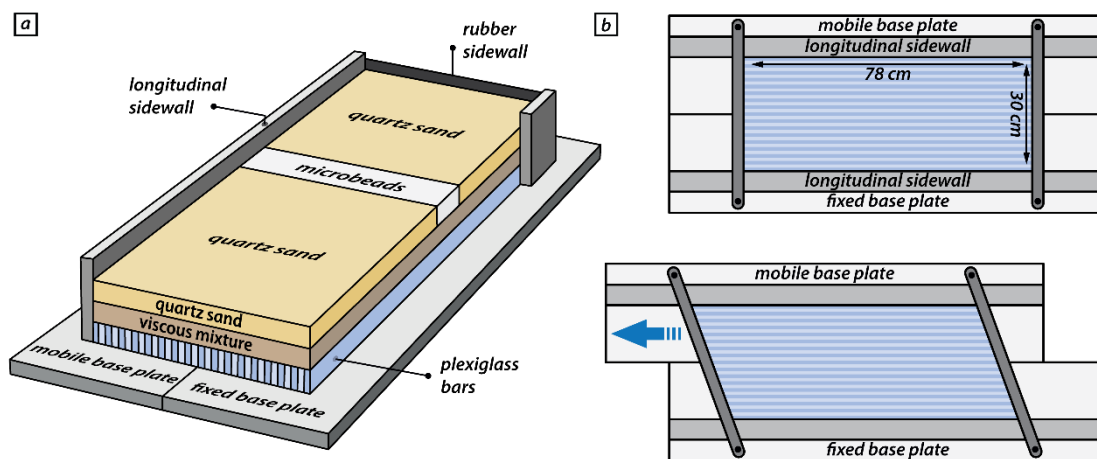
76 **2.1. Analogue model setup**

77 The experimental set-up for simulating distributed strike-slip shear included a mobile base plate that could
78 be translated horizontally above a fixed base plate (Fig. 1). An assemblage of 60 individual and moveable
79 plexiglass bars (each 78 cm long, 5 cm high and 5 mm wide) was positioned on top of two base plates. The
80 assemblage of plexiglass bars was confined by carbon-fiber sidewalls on the long sides (Fig. 1b) and
81 wooden bars (c. 5 mm high, 2 cm wide and 40 cm long) on the short sides (Fig. 1b, c), that could pivot
82 below the longitudinal sidewalls. The model was constructed on top of the plexiglass bars and consisted of
83 a 2 cm-thick viscous layer, simulating the ductile lower crust, overlain by a 2 cm-thick layer of granular
84 materials simulating the brittle upper crust. The short sides of the model were confined by vertical rubber

85 sheets. Although our model set-up included both a horizontal viscous layer overlain by a horizontal brittle
 86 layer, our experiments focus on the influence of vertical domains with brittle strength contrasts on strike-
 87 slip faulting. The function of the viscous layer, directly overlying the plexiglass bars, is to distribute the
 88 applied shear deformation over the entire width of the model in the overlying brittle layer (e.g. Schreurs,
 89 1991, 2003; Dooley and Schreurs, 2012).

90 Each model had an initial rectangular shape in map view, with a length of 78 cm parallel to the shear
 91 direction and a width of 30 cm perpendicular to it. The movement of the mobile base plate occurred by
 92 computer-controlled stepper motors at a constant velocity of 40 mm/h, resulting in 80 mm of total
 93 displacement after two hours. Displacement of the mobile base plate changed the initial rectangular shape
 94 of the overlying assemblage of plexiglass bars into a parallelogram simulating simple shear.

95



96

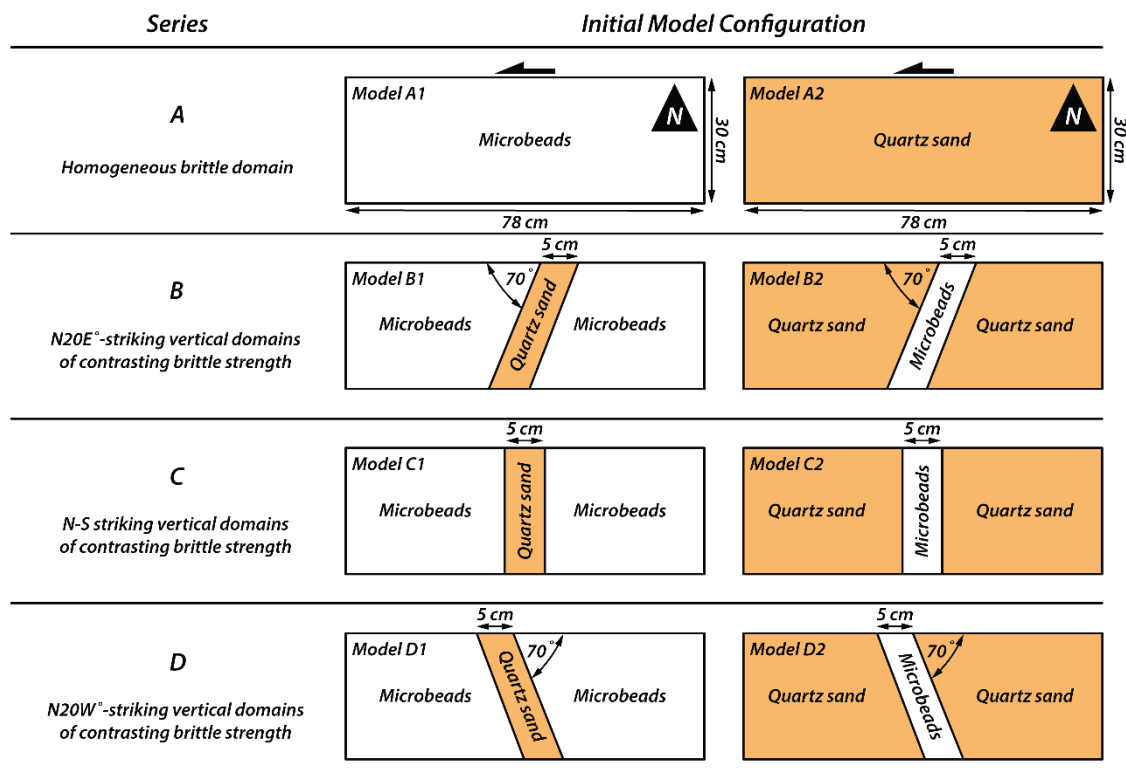
97 **Figure 1: Schematic experimental setup.** (a) The base of the model set-up consists of a fixed plate and a mobile
 98 plate overlain by an assemblage of individual and moveable plexiglass bars. The model is constructed on top of
 99 the plexiglass bars and is confined by two longitudinal sidewalls and two short sidewalls consisting of rubber
 100 sheets. (b) upper panel: Initial position of base plates overlain by plexiglass bars confined on the short sides by
 101 wooden bars that can pivot about a vertical axis; lower panel: Sinistral horizontal displacement of the mobile
 102 base plate induces a simple shear movement in the overlying assemblage of plexiglass bars as they slide past one
 103 another.

104

105 We performed four series of simple shear experiments, referred to as Series A, B, C and D (Fig. 2). Series
 106 A involved two models with only one brittle material (Fig. 2a), quartz sand or microbeads, to investigate
 107 strike-slip fault kinematics in a homogeneous upper crust, without any lateral variations in mechanical
 108 strength. In the other three series (Fig. 2b-d), we introduced vertical domain boundaries across which the

109 mechanical strength varied laterally. Each model had three domains with a 5-cm-wide central domain
 110 consisting of a different material than the domains on either side. The difference between Series B, C and
 111 D is the orientation of the central domain with respect to the shear direction. To achieve such a model set-
 112 up, two vertical thin sheets of cardboard (< 1 mm) were first placed as provisional walls, spaced 5 cm apart,
 113 on top of the viscous layer in the central domain of the model, parallel to the required orientation of the
 114 vertical domain boundaries. Subsequently, the different granular materials were sieved on top of the viscous
 115 layer and once the desired model thickness was reached, the cardboard sheets were carefully removed.
 116 Although removal of the cardboard produced increased dilation along a narrow zone, it hardly affects the
 117 de facto function of this vertical boundary as a primary surface with materials of contrasting brittle strength
 118 on either side. For descriptive purposes, we defined a North direction, which is perpendicular to the applied
 119 shear direction and parallel to the short sides of the undeformed model (Fig. 2a). In models with a brittle
 120 strength contrast, we can distinguish two outer domains, a western and an eastern one, and a central domain
 121 (Fig. 2b-d).

122



123
 124
 125
 126
 127
 128

Figure 2: Schematic drawing of the materials used and their surface distribution at the initial stage. All models have a length of 78 and a width of 30 cm. The references about the patterns observed have been given by using the long side of the edge of the models as “north”. In the series of models referred as A, only one type of material (quartz sand or microbeads) has been used. The diagrams of series B, C and D show the position and orientation of the vertical domain boundaries in plan view and which materials were used.

129 **2.2. Analogue materials**

130 We used two different types of granular materials in our analogue models to assess the role of vertical zones
 131 of contrasting mechanical strength in the upper crust: quartz sand and microbeads grains. The quartz sand
 132 (distributor Carlo Bernasconi AG; www.carloag.ch) has a grain size between 60 and 250 μm with a bulk
 133 density of 1560 kg m^{-3} , whereas the grain size of the microbeads (distributor: Worf Glasskugeln, Germany)
 134 lies between 150 and 210 μm with a bulk density of 1400 kg m^{-3} . These density values were achieved by
 135 sieving the granular material into the model box from a height of 30 cm. Both, quartz sand and microbeads
 136 deform according to the Coulomb failure criterion and have internal peak friction angles of 36° and 22° and
 137 cohesion values of $50 \pm 26 \text{ Pa}$ and $25 \pm 4 \text{ Pa}$, respectively (Panien et al., 2016; Schmid et al., 2020). The
 138 considerable difference in the internal peak friction angle between the two materials makes them suitable
 139 for simulating contrasting upper crustal rocks. According to their difference in the internal friction angle,
 140 we consider the microbeads and quartz sand as weak and strong materials, respectively.

141 The viscous layer in our models had a density of 1600 kgm^{-3} and consisted of a mixture of SGM-36
 142 polydimethylsiloxane (PDMS) and corundum sand (weight ratio of 0.965: 1.000). The mixture has a quasi-
 143 linear viscosity of $1.5 \times 10^5 \text{ Pa s}$ and a stress exponent of 1.05 (Zwaan et al., 2018). The properties of all
 144 analogue materials are summarized in Table 1.

145

146

Granular materials	Quartz sand	Microbeads	Viscous material	PDMS/corundum mixture
Density (kg/m^3)	1560	1400	Density (kg/m^3)	1600
Grain size (μm)	60-250	150-210	Viscosity (Pa s)	1.5×10^5
Peak friction coefficient μ and angle, ϕ	$0.72 - 36^\circ$	$0.41 - 22^\circ$	Stress exponent n	1.05
Cohesion (Pa)	50 ± 26	25 ± 4		

147 **Table 1:** Materials properties of used granular and viscous materials (after Panien et al., 2006; Schmid et al., 2020).

148

149 **2.3. Scaling**

150 For brittle Mohr-Coulomb type materials, dynamic similarity is given by the equation for stress ratios

$$\sigma^* = \rho^* g^* h^* \quad (1),$$

151 where ρ^* , g^* and h^* are the ratios of model to nature for density, gravity and length, respectively. Note,
152 that our two used granular materials have different densities, cohesions and internal friction coefficients.
153 However, the resulting scaling factors are nearly identical and therefore we provide only the scaling factors
154 for quartz sand. Where scaling factors substantially differ, we denote them with subscripts “qtz” and “mb”
155 for quartz sand and microbeads, respectively. Our model setup yields a length scaling factor of $h^* =$
156 2×10^{-6} and a gravity scaling factor of 1. For quartz sand, the density scaling factor is $\rho_{qtz}^* \sim 0.6$ and the
157 cohesion factor is $C_{qtz}^* = 1 \times 10^{-6}$ (using a cohesion of ~ 50 Pa and 50 MPa for our quartz sand and upper
158 crustal rocks, respectively; Byerlee, 1978). Additionally, for microbeads the density scaling factor and
159 cohesion scaling factor are $\rho_{mb}^* \sim 0.5$ and $C_{mb}^* = 1 \times 10^{-6}$ (assuming a weakened natural rock type with a
160 cohesion of c. 25 MPa), respectively. Using these scaling factors yields a stress scaling factor of $\sigma^* =$
161 1×10^{-6} for both quartz sand and microbeads.

162 Assuming a lower crustal viscosity of $\eta = 10^{22}$ Pa s (Moore and Parsons, 2015; Zhang and Sagiya, 2017)
163 yields a viscosity ratio $\eta^* = 1 * 10^{-17}$ (using the viscosity of $1.5 * 10^5$ Pa s for the viscous analogue
164 material).

165 The strain rate ratio is obtained from the stress ratio and the viscosity ratio by (Weijermars and Schmeling,
166 1986):

$$\dot{\epsilon}^* = \frac{\sigma^*}{\eta^*} \quad (2).$$

167 Note that due to the simple shear setup, we substitute the strain rate scaling factor $\dot{\epsilon}^*$ with the shear strain
168 rate scaling factor $\dot{\gamma}^* = 1 \times 10^{11}$. Next, the velocity scaling factor v^* and a time scaling factor t^* are
169 calculated with

$$\dot{\gamma}^* = \frac{v^*}{h^*} = \frac{1}{t^*} \quad (3)$$

170 yielding a velocity scaling factor $v^* = 2 \times 10^5$ and a time scaling factor $t^* = 1 \times 10^{-11}$.

171 Based on our scaling, 1 cm in our experiments corresponds to 5 km in nature and the applied velocity of 40
 172 mm h⁻¹ converts to a velocity of ~2 mm a⁻¹ in nature. Using the shear strain rate scaling factor $\dot{\gamma}^*$, the bulk
 173 shear strain rate $\dot{\gamma} = 3.7 \times 10^{-5} \text{ s}^{-1}$ in our models translates to a shear strain rate of $\dot{\gamma} = 3.7 \times 10^{-16} \text{ s}^{-1}$
 174 in nature and 1 h in our analogue experiments translates to ~12.5 Myr in nature.

175 In order to verify dynamic similarity of brittle natural and experimental material we calculate the
 176 Smoluchowski number S_m , which is the ratio between gravitational stress and cohesive strength (Ramberg,
 177 1981):

$$S_m = \frac{\rho gh}{C + \mu \rho gh} \quad (4),$$

178 where ρ , h , C and μ are the density, thickness, cohesion, and friction coefficient, respectively of the brittle
 179 material. With a cohesion of 50 MPa and a friction coefficient of ~0.6 (Byerlee, 1978) for upper crustal
 180 rocks, this yields values of $S_m \sim 1$ for our models as well as for nature. We further calculate the Ramberg
 181 number R_m to ensure dynamic and kinematic similarities between the viscous layers.

$$R_m = \frac{\rho gh^2}{\eta v} \quad (5)$$

182 For our velocity of 40 mm h⁻¹, this yields a Ramberg number of 6 for both, our models and nature. The
 183 Reynolds number R_e is defined as the ratio between inertial forces and viscous forces and is for all our
 184 models as well as for the natural prototype $\ll 1$:

$$R_e = \frac{\rho v h}{\eta} \quad (6)$$

185 Based on the applied scaling laws, the material properties and the similar non-dimensional numbers for
 186 model and nature, we consider our models to be properly dynamically scaled. Model parameters and
 187 dynamic numbers of the used materials are specified in Table 2.

188

	General parameters			Brittle upper crust		Ductile lower crust		Dimensionless numbers		
	Gravity [m/s ²]	Crustal thickness [m]	Shear velocity [m/s]	Density [kg/m ³]	Cohesion [Pa]	Density [kg/m ³]	Viscosity [Pa s]	Smoluchowski Sm	Ramberg Rm ¹	Reynolds Re
Model	9.81	4 x 10 ⁻²	1.1 x 10 ⁻⁶	1560	50	1600	1.5 x 10 ⁵	1	6	<<1
Nature	9.81	2 x 10 ⁴	6.3 x 10 ⁻¹¹	2700	5 x 10 ⁷	2900	1 x 10 ²²	1	6	<<1
Scaling ratios $x^* = x^m/x^n$ [dimensionless]										
	σ^*	ρ^*	g^*	h^*	C^*	$\dot{\gamma}^*$	η^*	v^*	t^*	
	1 x 10 ⁻⁶	0.5 ¹ -0.6	1	2 x 10 ⁻⁶	5 ¹ -10 x 10 ⁻⁷	1 x 10 ¹¹	1 x 10 ⁻¹⁷	2 x 10 ⁵	1 x 10 ⁻¹¹	

189 ¹ Lower values for scaling factors ρ^* and C^* refer to microbeads.

190 **Table 2:** Scaling parameters and scaling factors.

191

192

193

194 **2.4. Deformation monitoring and quantification**

195 Since the experiments were conducted using a simple shear setup, vertical motions during deformation
 196 were negligible, with nearly all movement located within the horizontal plane. The different experiments
 197 were monitored by an automated Nikon D810 (36 MPx) DSLR camera positioned above the experimental
 198 model. Images were taken at fixed intervals of 60 s during two hours, resulting in 121 subsequent top view
 199 images of the model surface. For a quantitative 2D analysis of the surface deformation, we used the
 200 StrainMaster module of the LaVision© DaVis image correlation software. Using a calibration plate, the
 201 software corrects the top view images for lens distortion effects (i.e., unwarping), applies image
 202 rectification and provides a scaling function that maps coordinates from the camera sensor to physical
 203 coordinates with a resolution of ~9 px/mm. The digital image correlation calculates local displacement
 204 vectors on subsequent images using a square matching algorithm with adaptive multi-pass cross-
 205 correlation. To properly track the grain movement patterns, we sprinkled coffee grains on the model surface
 206 prior to the model run. For each image, the analyzed area is subdivided into small interrogation window for
 207 which a local displacement vector is determined by cross-correlation. We used subsets (i.e., interrogation
 208 windows) of 31 by 31 pixels with a 75% overlap for the local displacement calculations that, assembled

209 result in incremental (60 s interval) displacement fields for the horizontal x- and y-components u_x and u_y ,
210 respectively with a vector resolution of ~ 1.3 vectors/mm.

211 Postprocessing included an outlier filter to fill gaps of pixels within a 3 by 3 neighborhood (Westerweel
212 and Scarano, 2005). Discarded vectors in the displacement fields were replaced by an iterative interpolation
213 requiring at least two neighboring vectors. For quantifying deformation at the model surface, we calculate
214 the z-vorticity ω_z (i.e., a rotation measure in the xy plane) as a proxy for shear movement along strike-slip
215 faults. In our models the X-axis corresponds to the long side of the rectangle; and the Y-axis corresponds
216 to the short side of the model. In contrast to the shear strain ϵ_{xy} , vorticity is not dependent on the orientation
217 of the coordinate system, which is crucial when quantifying deformation along faults that strike obliquely
218 with respect to the coordinate system (e.g., Cooke et al., 2020). ω_z can be derived from local displacement
219 gradients according to equation 1:

$$\omega_z = \frac{\partial u_y}{\partial x} - \frac{\partial u_x}{\partial y} \quad (7)$$

220 With u_x and u_y being the horizontal displacement components in the x, and y direction, respectively. Positive
221 and negative ω_z values refer to sinistral and dextral relative displacement, respectively. Within the
222 predefined increment of 60 s, ω_z values are consistently within the range [-2%, 2%] and we set a threshold
223 of -0.5% and 0.5% to distinguish between active deformation and background noise for dextral and sinistral
224 shear sense, respectively. In the results section we present ω_z at deformation stages every 30 min (i.e., after
225 30, 60, 90, and 120 min). Finite deformation after 120 min for each model is illustrated with a surface
226 photograph and enhanced with superposed line drawings of the fault pattern. For the statistical analysis of
227 fault orientations, we traced active fault segments (i.e., $\omega_z \leq -0.5\%$ or $\omega_z \geq 0.5\%$) in MATLAB using
228 polylines, where each fault segment is defined by two consecutive vertices. At each time step, segment
229 length and azimuth were calculated and visualized in length-weighted rose diagrams.

230

231

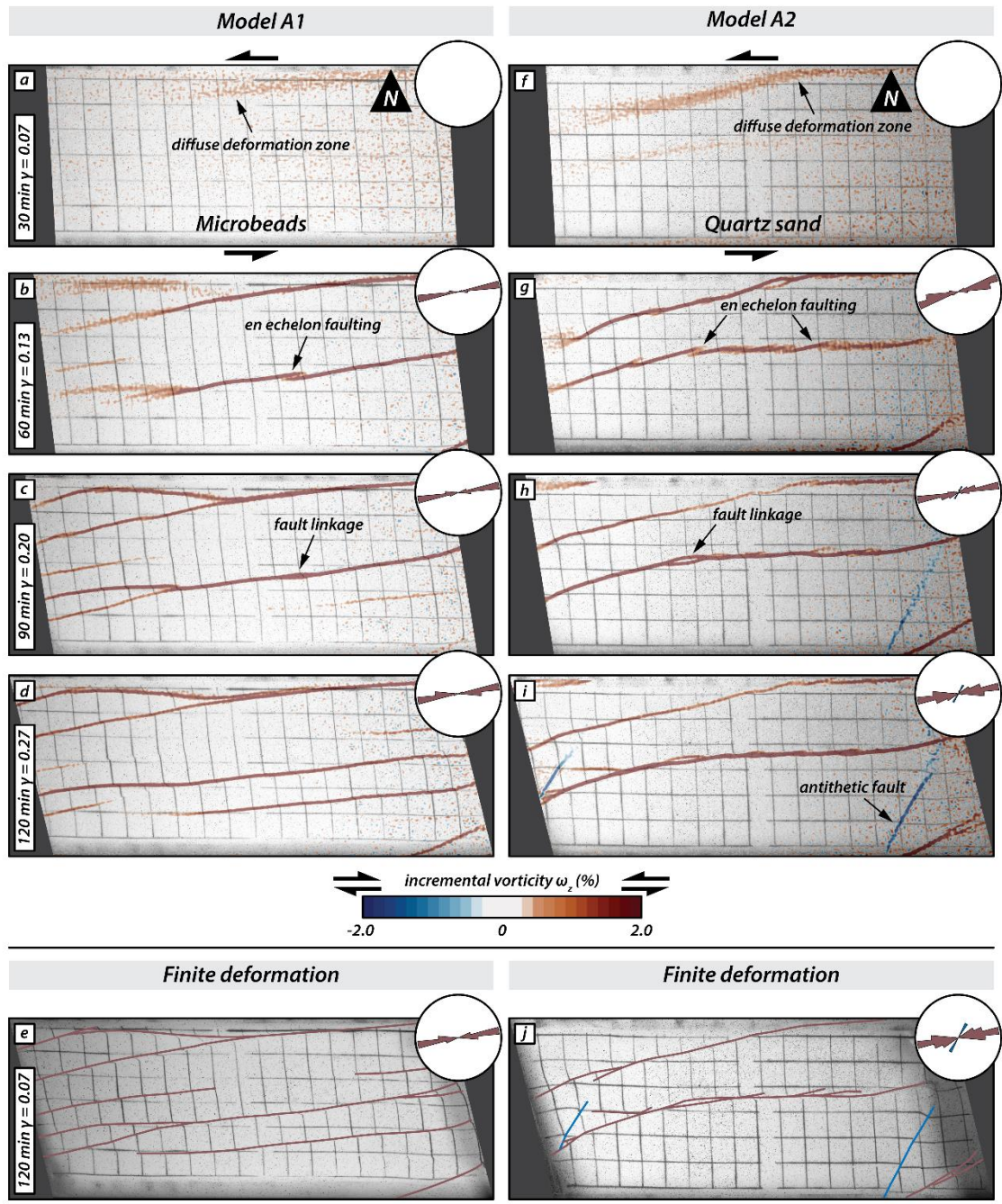
232

233 **3. Results**

234 **3.1. Series A: Fault evolution in a homogeneous upper crust**

235 The Series A models consisted of a homogeneous upper crustal layer composed of either microbeads (Fig.
236 3; Model A1) or quartz sand (Fig. 3; Model A2). The incremental strain panels document that strain
237 localized first in the model with quartz sand, while deformation was still diffuse in the model with
238 microbeads (Fig. 3a and f), i.e. strain localization occurs at lower amounts of applied simple shear in quartz
239 sand than in microbeads. With progressive sinistral simple shear deformation, slightly overlapping right-
240 stepping *en echelon* strike-slip faults with a sinistral displacement formed (Fig. 3b and g). These faults were
241 synthetic with respect to the bulk simple shear. In the model with microbeads (Model A1) the first synthetic
242 faults had an orientation of N79°E (Fig. 3b), whereas in the model with quartz sand (Model A2) their
243 orientation was N72°E (Fig. 3g). Initial deformation in both models is accommodated by synthetic
244 (sinistral) strike-slip faults (Fig. 3a, b and f, g). As deformation progressed, individual fault segments linked
245 up forming major sinistral strike-slip faults (Fig 3c and h). Antithetic faults only developed in Model A2
246 (quartz sand only; Fig. 3h and i) at later stages of deformation. These faults were confined in between
247 previously formed synthetic faults. The final deformation stage (Fig. 3e and j) shows that most deformation
248 was taken up by major synthetic faults that crossed the entire length of the model. At the final stage, the
249 initial *en echelon* pattern of faulting was better preserved in the quartz sand model than in the microbeads
250 model, resulting in a wider damage zone in the former.

251



252

253 Figure 3: Overview of Series A models: Simple shear deformation of two models with a homogenous upper
 254 brittle layer. The first four panels of each series show surface photographs with the incremental vorticity after
 255 30 minutes (20 mm displacement of mobile base plate), 60 minutes (or 40 mm displacement), 90 minutes (or 60
 256 mm displacement) and 120 minutes (or 80 mm displacement). Incremental positive and negative values indicate
 257 sinistral (synthetic, red) and dextral (antithetic, blue) relative movement, respectively. The last panel for each
 258 series shows a surface photograph of the final stage overlain with the interpreted fault pattern; red lines are
 259 sinistral faults, blue lines are dextral faults.

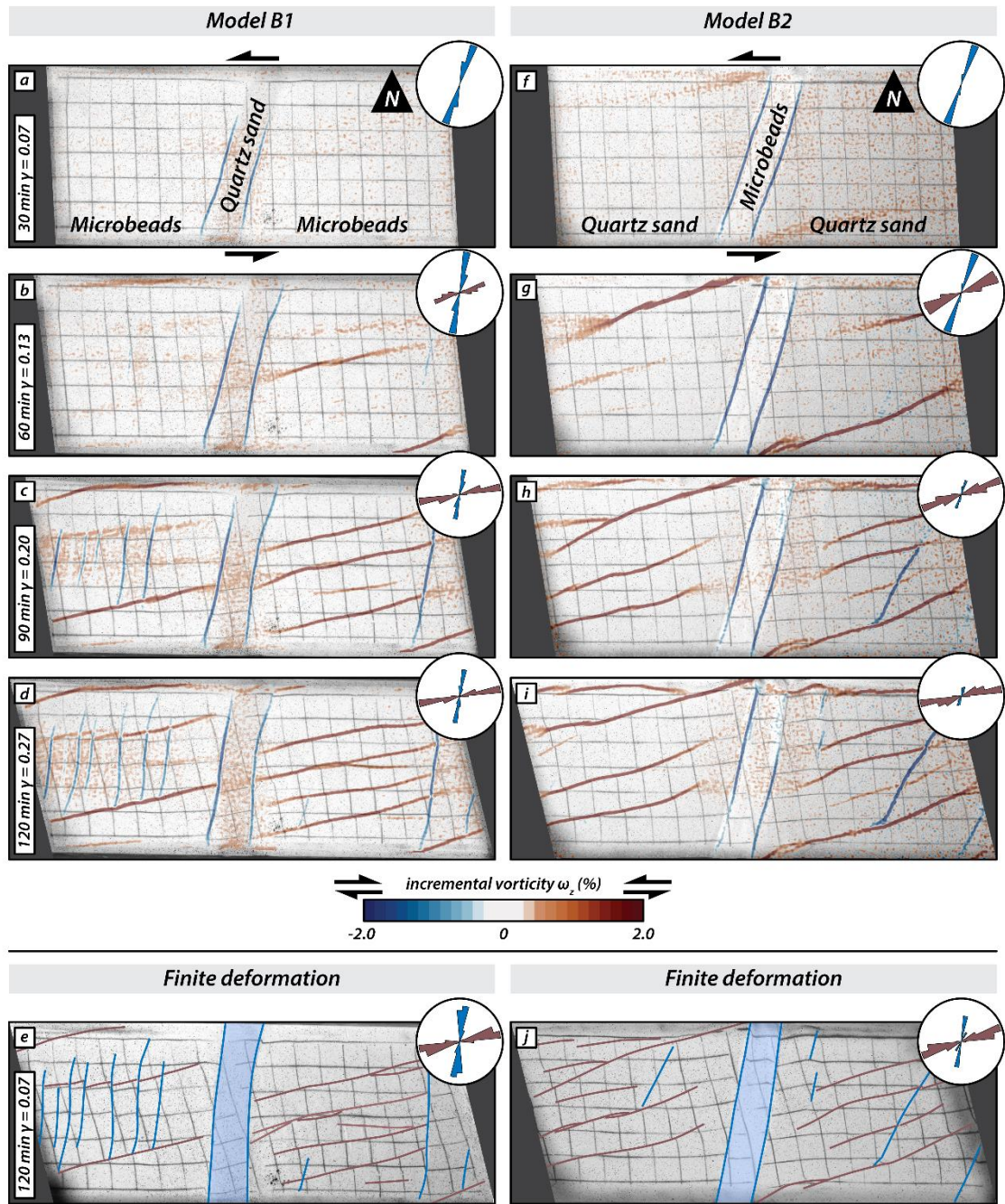
260

261

262

263 **3.2. Series B: Fault evolution in models with N20°E vertical domain boundaries**

264 The vertical domain boundaries in the Series B models were oriented N20°E. Model B1 had a central
265 domain consisting of strong quartz sand with weak microbeads in the adjacent, western and eastern domains
266 (Fig. 4; Model B1), whereas in Model B2 it was the other way around. (Fig. 4; Model B2). Both models
267 showed the development of dextral strike-slip (antithetic, with respect to sinistral simple shearing) faults
268 along the vertical boundaries of the central domain (Fig. 4a, f). Later, sinistral strike-slip faults (synthetic)
269 formed in the western and eastern domains (4b, g). Although these faults propagated laterally with time,
270 none of the synthetic faults crossed the central domain. Instead, they halted at or close to the boundary
271 faults along the central domain (Fig. 4c, h). In Model B1 a few antithetic faults formed in between pre-
272 existing synthetic faults in the western and eastern domains, striking at c. N60°E (Fig. 4d, e). Antithetic
273 faults developed also in the western and eastern domains of Model B2, almost coevally with the synthetic
274 faults. They strike at higher angles to the shear direction than those antithetic faults confined between
275 overlapping synthetic faults in Model B2. With increasing deformation, the central domain and its bordering
276 antithetic faults rotated counterclockwise in both models (Fig. 4a-e, f-j), as did the antithetic faults in the
277 western and eastern domains, which acquired a slight sigmoidal shape form (e.g. Fig. 4j)



278

279 **Figure 4: Overview of Series B models: Simple shear deformation of two models with vertical domains of**
 280 **contrasting brittle strength oriented N20°E. The first four panels of each series show surface photographs with**
 281 **the incremental vorticity after 30 minutes (20 mm displacement of mobile base plate), 60 minutes (or 40 mm**
 282 **displacement), 90 minutes (or 60 mm displacement) and 120 minutes (or 80 mm displacement). Incremental**
 283 **positive and negative values indicate sinistral (synthetic, red) and dextral (antithetic, blue) relative movement,**
 284 **respectively. The last panel for each series shows a surface photograph of the final stage overlain with the**
 285 **interpreted fault pattern; red lines are sinistral faults, blue lines are dextral faults.**

286

287

288

289

290

3.3. Series C: Fault evolution in models with N-S vertical domain boundaries

291

During the early stages of simple shear, dextral (antithetic) faults formed along the N-S striking borders of

292

the central domain (Fig. 5b, g) in both models, but earlier and more pronounced in Model C1. With

293

progressive shearing, both synthetic and antithetic faults formed in the outer domains of both models (Fig.

294

5c and h). In Model C2, activity along the antithetic faults bordering the central domain ceased, and

295

synthetic faults propagated from the outer domains into the central weak domain (Fig. 5h-j). In contrast, in

296

Model C1, the antithetic faults along the borders of the central domain remained active, and no synthetic

297

faults crossed the central strong domain (Fig. 5d). In the eastern domain of Model C2, a few antithetic faults

298

formed in between major synthetic faults, striking at a lower angle to the shear direction than earlier formed

299

antithetic faults in the western domain. With progressive simple shear the central domain showed

300

counterclockwise rotation around a vertical axis in both models and antithetic faults obtained a sigmoidal

301

shape in top view (Fig. 5i). As the initial N-S antithetic faults bordering the central domain rotated

302

counterclockwise, activity along these faults stopped and new fault segments parallel to earlier antithetic

303

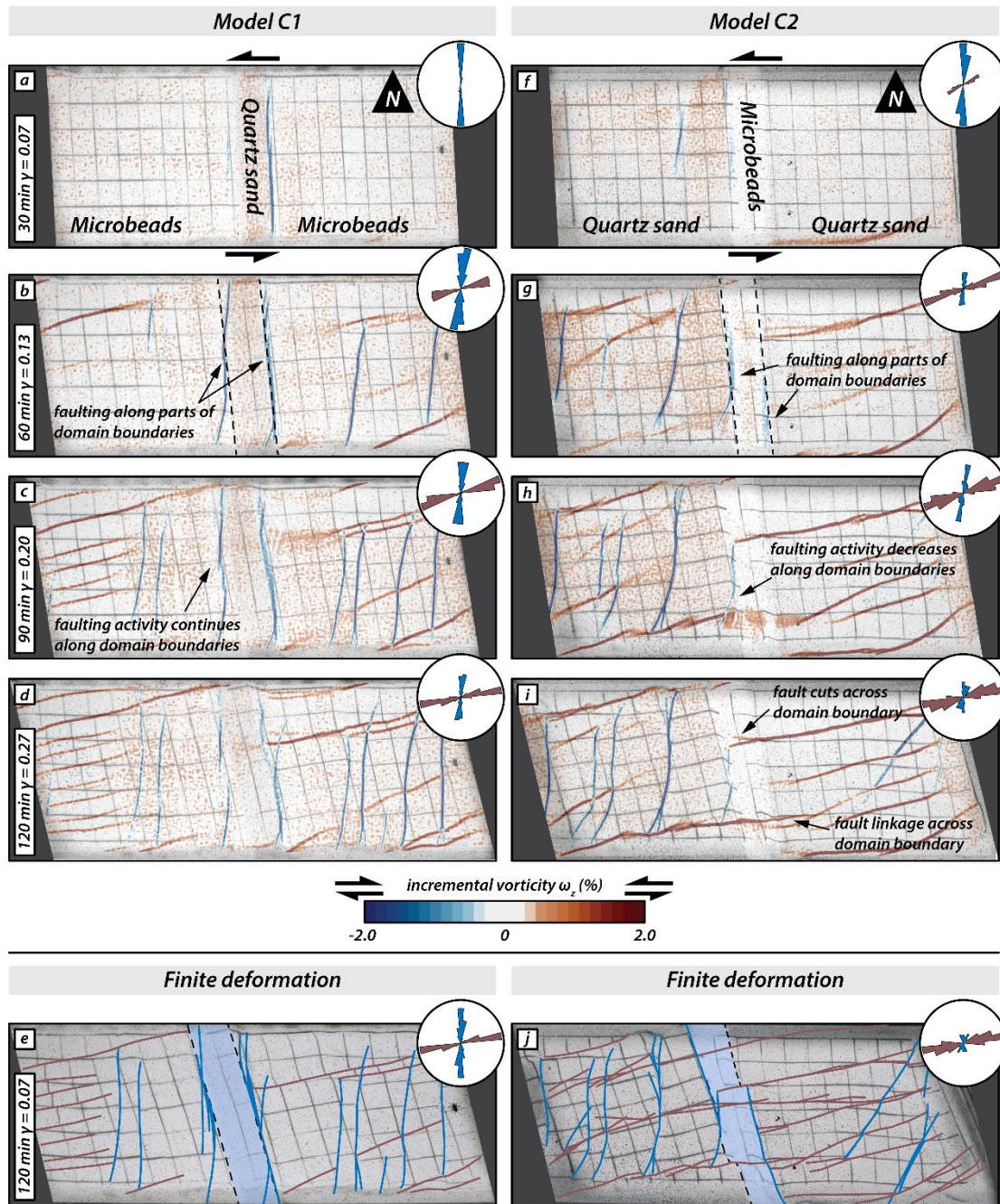
faults formed in the western and eastern domains (Fig. 5d, e). At the final stage of Model C2, antithetic

304

faults dominated in the western domain and synthetic faults in the eastern domain. In contrast, in Model

305

C1, antithetic and synthetic faults were present in both the western and eastern domain.



306

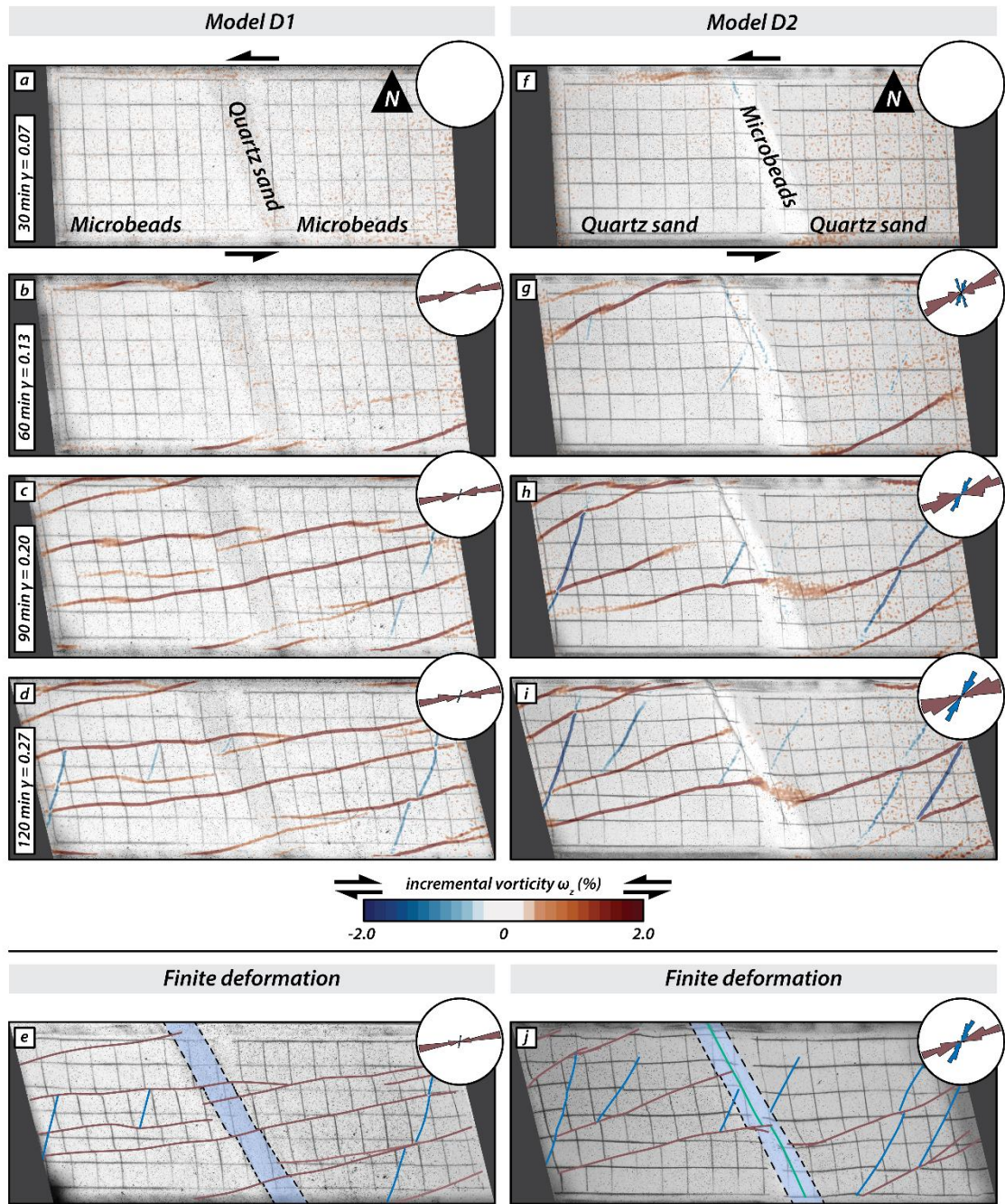
307 **Figure 5: Overview of Series C models: Simple shear deformation of two models with vertical domains of contrasting brittle strength striking N-S. The first four panels of each series show surface photographs with the**
 308 **incremental vorticity after 30 minutes (equivalent to 20 mm displacement of the mobile base plate), 60 minutes**
 309 **(or 40 mm displacement), 90 minutes (or 60 mm displacement) and 120 minutes (or 80 mm displacement).**
 310 **Incremental positive and negative values indicate sinistral (synthetic, red) and dextral (antithetic, blue) relative**
 311 **movement, respectively. The last panel for each series shows a surface photograph of the final stage overlain by**
 312 **the interpreted fault pattern; red lines are sinistral faults, blue lines are dextral faults.**
 313

314

315

316 **3.4. Series D: Fault evolution in models with N20°W striking vertical domain boundaries**

317 In contrast to the Model C series, no faults formed along the boundaries of the central domain in both
318 Models D1 and D2 (Fig. 6a and f). Model D1 is dominated by synthetic faults crosscutting the central strong
319 domain (6c-e). As these faults traversed the central domain, they slightly changed their strike. In contrast,
320 in Model D2 the weak microbeads of the central domain were internally deformed and oblique-slip reverse
321 faults formed, which propagated laterally and parallel to the domain boundaries (Fig. 6g-j). Synthetic faults
322 formed both in the western and eastern domain of Model D2, while antithetic faults formed later and in
323 between overlapping synthetic faults (Fig. 6g-j). With progressive deformation synthetic faults from the
324 western and eastern domain in Model D2 propagated partially into the central, weak central domain, but
325 halted at the previously formed oblique-slip reverse faults (Fig. 6h and i). During late stages of deformation
326 a few antithetic faults formed in Model D1 in between earlier formed synthetic faults, striking at larger
327 angles to the shear direction than in Model D2.



328

329 Figure 6: Overview of Series D models: Simple shear deformation of two models with N20°W striking vertical
 330 domains of contrasting brittle strength. The first four panels of each series show surface photographs with the
 331 incremental vorticity after 30 minutes (20 mm displacement of mobile base plate), 60 minutes (or 40 mm
 332 displacement), 90 minutes (or 60 mm displacement) and 120 minutes (or 80 mm displacement). Incremental
 333 positive and negative values indicate sinistral (synthetic, red) and dextral (antithetic, blue) relative movement,
 334 respectively. The last panel for each series shows a surface photograph of the final stage overlain with the
 335 interpreted fault pattern; red lines are sinistral faults, blue lines are dextral faults, green line indicates reverse
 336 fault.

337

338

339

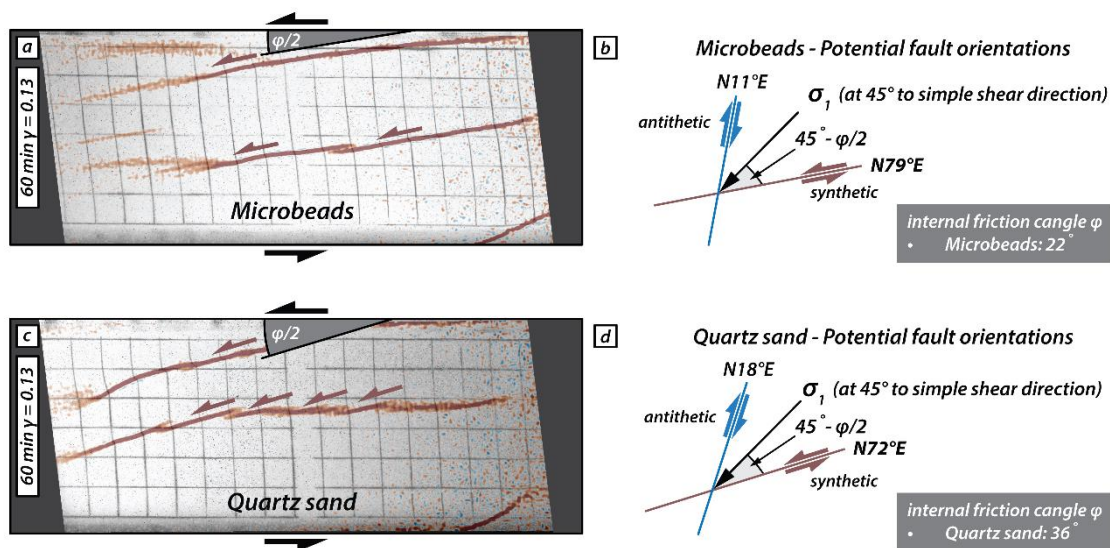
340 **4. Discussion**

341 **4.1. Series A: Strike-slip faulting in models with a homogeneous upper crust model**

342 In our models simulating homogeneous crust the structures display an *en echelon* pattern, as should be
343 expected (Bartlett et al., 1981; Sylvester, 1988; Misra et al., 2009). Initial bulk simple shear is
344 accommodated in both models by zones of diffuse deformation and is followed by localized deformation
345 along narrow fault zones. It is interesting to note that localization requires a higher shear deformation in
346 the model with the weak material than in the model with strong material. This difference in localization
347 behaviour is attributed to the difference in dilatancy between the two analogue materials, which is closely
348 related to grain shape and grain size distribution. The weak material, represented by the microbeads, are
349 well-rounded and have a narrow grain size distribution (150-210 μm), whereas the strong material (quartz
350 sand grains) is angular and have a wider grain size distribution (60-250 μm). The more uniform the grain
351 shape and grain size, the more applied shear deformation is needed to localize the strain along a narrow
352 fault zone (Antonellini et al., 1995; Mair et al., 2002). Therefore, the shape and grain-size characteristics
353 will influence the time that a fault may take to reactivate depending on the lithology that comprises its fault
354 zone (e.g. Sammis et al., 1987; Mair et al., 2002).

355 In these two models sinistral (synthetic) strike-slip faults form first. The initial strike of these faults differs
356 between the model with the weaker material and the one with strong material, striking at N79°E and N72°E,
357 respectively. The internal friction angle of each type of material will be adjusted to a certain orientation of
358 rupture according to the Mohr-Coulomb criterion. (Fig. 7). At the beginning of the experiment, the main
359 principal stress (σ_1) is oriented at 45° to the shear direction, and the two potential fault orientations strike
360 at $45^\circ - \phi/2$ and at $45^\circ + \phi/2$ to σ_1 , respectively with ϕ the angle of internal peak friction, which is 22°
361 for the microbeads and 36° for quartz sand (Fig. 7). Hence, the synthetic and antithetic faults strike at N79°E
362 and N11°E, respectively in the model with microbeads and at N72°E and N18°E in the model with quartz
363 sand respectively. The fact that nearly all deformation is accommodated by synthetic faults is typical of
364 simple shear models with an initial rectangular shape, i.e. a large aspect ratio of length (parallel to shear
365 direction) divided by width (Schreurs, 2003; Dooley & Schreurs, 2012). A comparison of previous simple
366 shear experiments shows that the shape of the initial model has an influence on the relative proportion of
367 synthetic and antithetic faults (Gapais et al., 1991; Schreurs, 2003). With decreasing aspect ratio, the
368 number of antithetic faults will increase, and in case of an initially square-shaped model, (i.e., aspect ratio

369 is 1) antithetic faults will dominate (Gapais et al., 1991; Dooley & Schreurs, 2012). In the model with
 370 quartz sand, a few antithetic faults form in between previously formed major synthetic faults (Fig. 3i).
 371 These late antithetic faults, however, form in response to local stress field modifications between
 372 overlapping synthetic faults, causing σ_1 to rotate clockwise from 45° to the bulk shear direction towards an
 373 orientation that is subparallel to the previously formed synthetic faults. As a consequence, these late
 374 antithetic faults are not in the “conjugate” position with respect to the synthetic major faults, but strike at
 375 lower angles with respect to the long borders of the model (these are the lower-angle antithetic faults of
 376 Schreurs, 2003).

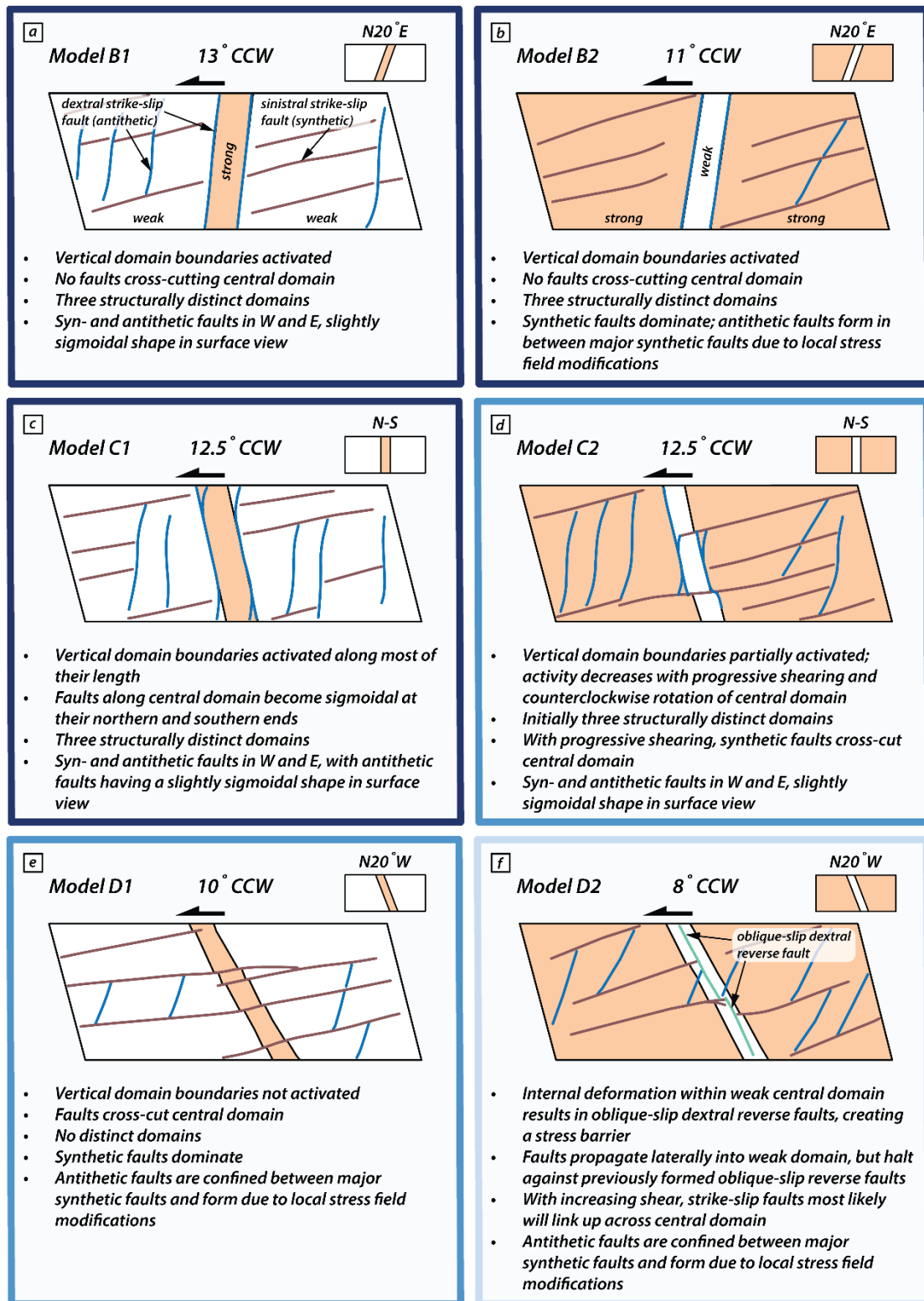


377
 378 **Figure 7: Illustrative scheme of the expected fault orientation according to the Mohr-Coulomb failure criteria,**
 379 **for the experiments with only one type of material (homogeneous upper crust). a) and c) Surface photographs**
 380 **of the model with microbeads only (a) and quartz sand only (c), with the incremental vorticity after 60 minutes**
 381 **(40 mm displacement). b) and d) Schematic explanation for the expected orientation of the synthetic and**
 382 **antithetic faults considering the simple shear orientation along with the Mohr-Coulomb failure criteria, for the**
 383 **models with microbeads and quartz sand only respectively.**

384

385 **4.2. Series B, C and D: The influence of the orientation lateral heterogeneities on strike-slip**
 386 **faulting**

387 Introducing a vertical domain with different properties than the surrounding material results in different
 388 fault patterns and timing of the structures (Segall and Pollard, 1983; Peacock, 1991; Peacock and
 389 Sanderson, 1992; Schellart and Strak, 2016; Lefevre et al., 2020; Livio et al., 2019; Venancio and Alves Da
 390 Silva, 2023). The degree of difference in the fault pattern is a function of the orientation and the strength
 391 of the domains.



392

393 Figure 8: Schematic surface views summarizing the main results from the models with vertical domains of
 394 contrasting brittle strength.

395

396 The first thing noticed is that the faults do not follow the *en echelon* pattern and the antithetic faults are the
397 first one to be form (Figs. 4 and 5). The domain boundaries in Series B and C models initially strike N20°E
398 and N-S respectively (Fig. 8a, b, c and d), which is close to the antithetic fault orientation predicted by the
399 Mohr-Coulomb failure criterion (i.e. N11°E for microbeads and N18°E for quartz sand, see section 4.1).
400 As a result, the domain boundaries in both models are activated along their entire length, and the antithetic
401 faults are formed along the borders of the central domains (Fig. 8a, b and c). With progressive sinistral
402 simple shear, the central domain bounded by the fault rotates counterclockwise about a vertical axis and, at
403 the end of the experiment has rotated about 12° striking N08°E. The faults of the domain boundaries remain
404 active throughout the model run, because their strike is favorably oriented respect the main stress (Fig 8a,
405 b). As a result the sinistral faults in the series B and in model C1 cannot propagate along the entire model,
406 regardless of the composition of the central domain, and two possibilities are shown: the faults are
407 segmented (Fig 8a and b) or more new faults are generated in the eastern and western domains (Fig. 8c).
408 However, if the central domain is composed of the weak material and is not fully surrounded by antithetical
409 faults, the synthetic fault can crosscut the entire model (Fig. 8d). This may offer the possibility that strike-
410 slip fault stepping may also be due to the action of lithology, which is able to induce fault segmentation.
411 Hence, the presence laterally heterogeneous upper crust with steep boundaries and suitable oriented for
412 activation by antithetic faults, can prevent the synthetic strike-slip faults from crossing certain domains.

413 The antithetic faults that form in the outer domains of our models are of two types: (i) those that form
414 relatively early in as yet largely unfaulted domains and strike at large angles to the shear direction (Fig. 8a,
415 c and d) and (ii) those confined between earlier formed and overlapping synthetic faults that strike at lower
416 angles to the shear direction (Fig. 8b, e and f). In the first case, the early-formed antithetic faults reflect the
417 orientation predicted by the Mohr-Coulomb failure criterion; striking N18°E if the outer domains consist
418 of the strong material and N11°E if the outer domains consist of the weak material. Due to lateral fault
419 propagation and coeval rotation of the central fault segments, these antithetic faults obtain a slightly
420 sigmoidal shape form in map view during progressive simple shear (see also Schreurs, 1994, 2003; Dooley
421 and Schreurs, 2012). In th second case, the antithetic faults confined in between closely spaced, earlier
422 formed, synthetic faults have an initial different strike (N15°-N20°E in the weak material, e.g. Model C1)
423 and N25°- N30°E in the strong material, (e.g. Model C2). The antithetic faults confined between major
424 synthetic faults result from local stress field modifications governed by relative movement of material in
425 between previously formed synthetic faults with large overlap (Schreurs, 2003; Dooley and Schreurs, 2012;

426 their R'_L faults). Both types of antithetic faults rotate counterclockwise with progressive sinistral simple
427 shear. Rotation of faults and blocks in strike-slip fault systems is not only observed in analogue models
428 (Schreurs, 1994, 2003; Dooley and Schreurs, 2012), but has also been documented in nature (e.g., Ron et
429 al., 1986; Nicholson et al., 1986). It is thus important to keep in mind that antithetic faults (and blocks in
430 between) can undergo considerable rotation about a vertical axis during simple shear deformation, implying
431 that present-day antithetic fault orientations in strike-slip fault systems do not necessarily reflect the
432 orientations in which they initially formed.

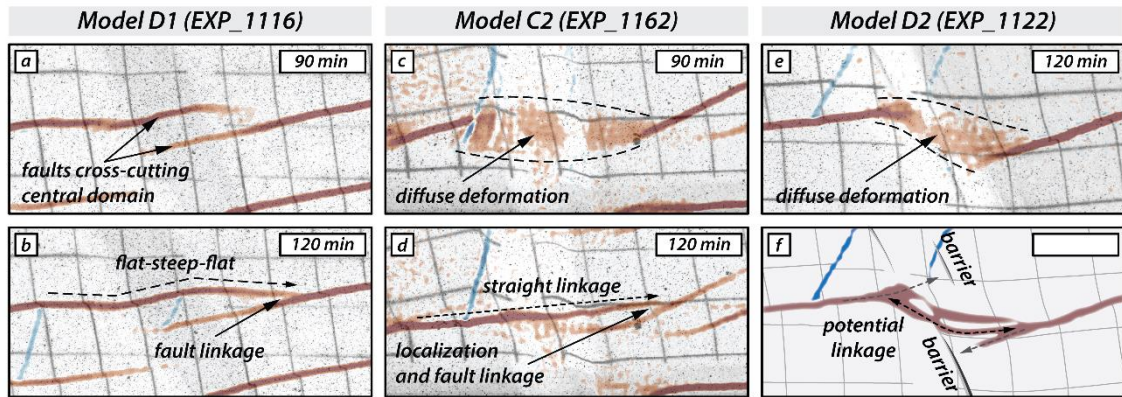
433 In comparison with the Series B and Series C models, the initial $N20^\circ W$ striking central domain boundaries
434 in the Series D models are the least favorably oriented for antithetical fault activation. Consequently, the
435 fault development pattern follows an echelon type, but in both cases the size of the segments is affected by
436 the lateral variation of the material properties. In the weak-strong-weak Model D1 (Fig. 8e and f), the
437 domain boundaries are not activated at all and the synthetic faults forming in the outer domains propagate
438 across the central domain. Apart from a slight re-orientation of the fault strike, reflecting the difference in
439 material strength between central and outer domains (difference in internal friction angles), the fault pattern
440 in Model D1 is similar to the one in Model A1, which had no vertical brittle strength contrasts. The strong-
441 weak-strong Model D2 shows a different deformation behaviour. Although the domain boundaries at the
442 surface are not activated, the presence of a weak material surrounded by strong material results in internal
443 deformation within the central domain and dextral oblique-slip reverse faults form striking parallel to the
444 domain boundaries. These faults prevent synthetic faults from crossing the central domain, and they halt
445 against the oblique-slip reverse faults.

446

447 **4.3. Fault linkage across central domain**

448 In models where synthetic faults from the eastern and western domain cross-cut the central domain, the
449 entire model behaves as one domain. As shown in the section above, this is the case for models C2, D1,
450 and D2 where the vertical boundaries of the central domain are not or only partially activated, depending
451 on the orientation of the central domain (section 4.2). However, all three models show distinct differences
452 in how laterally propagating synthetic strike-slip faults link across the central domain (Fig. 9). For model
453 D1 (Fig. 9a, b), faults cross-cut the stronger central domain from the eastern and western domains (Fig. 9a)

454 linking up in a new segment. This new segment shows different orientation resulting in a step-like linkage
 455 pattern in surface view (i.e., flat-steep-flat; Fig. 9a, b). When segmentation occurs and the faults cross the
 456 central domain, the orientation of the faults is different, probably related to the internal friction angles
 457 between the quartz sand and the microbeads (Du and Aydin, 1995; de Doney et al., 2011).



458

459 **Figure 9: Surface detailed photographs of the central domain of the models with the contrasting brittle**
 460 **mechanical strength, showing the fault linkage across the central domain at 90 minutes (60 mm displacement)**
 461 **and 120 minutes (80 mm displacement). a) and b) model D1 with the central domain striking N20°W and**
 462 **composed by the strong material (quartz). c) and d) model C2 with the central domain striking N-S and**
 463 **composed by the weak material (microbeads). e) model D2 with the central domain striking N20°W and**
 464 **composed by the weak material (microbeads). f) Schematic drawing for the fault linkage at the last stage.**

465

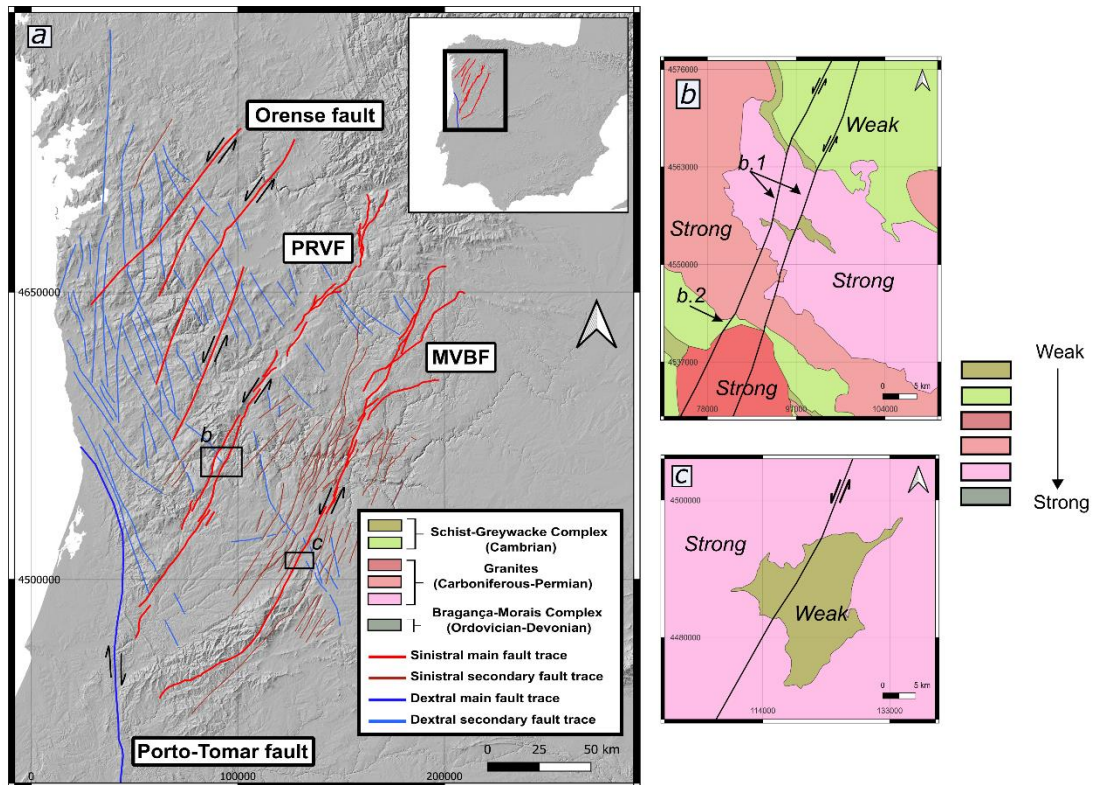
466 For models C2 and D2, however, the domain configuration strong-weak-strong has implications for fault
 467 linkage. As synthetic strike-slip faults propagate from the western and eastern domains towards the weaker
 468 central domain, early deformation patterns are characterized by a zone of diffuse deformation across the
 469 central domain (Fig. 9c, e). In model C2, the fault from the W domain cross-cuts the weak central domain
 470 and eventually links with the fault in the E domain in a straight fashion after 120 min (Fig. 9d), abandoning
 471 earlier active fault strands striking N18°E (i.e., the predicted orientation for Mohr-Coulomb failure
 472 criterion). Similar fault kinematics should be expected for model D2 (Fig. 9e, f). However, laterally
 473 propagating faults in the western and eastern domain do not link during the duration of the model run.
 474 Instead, the two fault segments halt at the domain boundary resulting in ongoing diffuse deformation
 475 without strain localization in the central domain. This behavior may be explained by the presence of the
 476 N20°W-striking reverse faults within the central model domain. Due to the misalignment between central
 477 domain boundaries and the expected orientation of antithetic faults, the domain boundaries do not activate
 478 and domain-internal deformation is taken up by oblique-slip dextral reverse faults. Such faults (i.e., nearly
 479 orthogonally striking with respect to synthetic faults) accommodate bulk shear deformation hindering the

480 synthetic faults to propagate. In that sense, the oblique-slip reverse faults act as an impenetrable barrier
481 inhibiting linkage of synthetic faults across the weak central domain (Fig. 9f). Oblique-slip reverse faults
482 in the central domain, therefore, influence fault interaction across the central domain in a similar way as do
483 the activated domain boundaries in models B1, B2, and C1 (Fig. 8).

484

485 **4.4. Comparison with strike-slip fault zones in Iberia**

486 The NW Iberian Peninsula contains major sinistral and dextral strike-slip intraplate fault systems (Fig. 10a).
487 These intraplate fault systems are located in an old basement developed during Variscan Orogeny
488 (Devonian-Carboniferous, e.g., Matte, 1991; Martínez Catalán et al., 1997; Fernández et al., 2004), during
489 this stage a set of lithologic units with contrasting properties such as granites, quartzites, slates and high-
490 grade metamorphic rocks were emplaced and deformed. During the Alpine Compression (Late Cretaceous
491 to the present), the present fault pattern was obtained due to the collision between the Iberian microplate
492 and the northern edge of Africa in the middle Miocene (e. g., Alonso et al., 1996; Vegas et al., 2004; Martín-
493 González and Heredia, 2011, Martín-González et al., 2012). This collision caused the Iberian Peninsula to
494 undergo a counterclockwise twist, resulting in slight shearing (e.g. Martínez Catalán, 2011; Vergés et al.,
495 2019). In the study area, intraplate deformation led to a fault pattern primarily composed of sinistral faults,
496 such as the Penacova-Régua-Verin (PRVF), Manteigas-Vilariça-Bragança (MVBF), and Orense faults (see
497 Fig. 10a). Additionally, antithetic dextral faults were also generated (see Fig. 10a).



498
 499 **Figure 10: a) Digital elevation model of the northwest section of the Iberian Peninsula where the main faults**
 500 **are drawn, with the location of Figures b and c. The faults are essentially sinistral and there is a dextral fault on**
 501 **the southern edge that delimits the study area. In blue and light red, the secondary antithetic (dextral) and**
 502 **synthetic (sinistral) faults have been marked respectively. b) Schematic representation of the southern section**
 503 **of the Verin fault showing patterns of directional changes similar to models D1 and D2. c) Schematic**
 504 **representation of the southern section of the Vilariça fault showing a similar deformation pattern to model C2.**

505

506 Among the traces of these faults, we can observe antithetic faults that do not connect with each other and,
 507 in some cases, acquire a sigmoidal as observed in Models C1 and C2 models (Fig. 8e and f). These antithetic
 508 faults are not in a conjugate position and mostly confined between major sinistral faults. At the end of the
 509 sinistral faults is the Porto-Tomar fault, which delimits the study area. The Porto-Tomar fault shows dextral
 510 displacement and tectonically delimits the area to the north and south of Portugal (Veludo et al., 2017). The
 511 main traces of the sinistral faults are not completely straight, but show slight changes in strike. For example,
 512 along the PRVF, the fault undergoes a counterclockwise refraction when crossing from weak into strong
 513 lithologies (b.1 in Fig. 10b), similar to Model D1 with strong quartz sand in the central domain (Fig. 10b).
 514 On the other hand, the same fault undergoes a clockwise refraction as it crosses from strong lithologies
 515 (granites) in shaly units (b.2 in Fig. 10b), similar to Model D2 with weak microbeads in the central domain.
 516 The same phenomenon is also observed along the Vilariça fault when the fault intersects granites and slate
 517 units (Fig. 10c).

518 Although on a local scale, similarities are observed in the behaviour of individual faults crossing contrasting
519 lithologies in nature and faults crossing vertical domain boundaries in our analogue models, the NW Iberian
520 Peninsula strike-slip fault system as a whole does show little resemblance with the overall fault patterns in
521 homogeneous or laterally heterogeneous upper crustal models. This may indicate that the NW Iberian crust
522 is much more heterogeneous and complex than the one modelled in our experiments.

523

524 **5. Conclusions**

525 We performed a series of analogue models to investigate faulting in the upper, brittle crust as a result of
526 sinistral simple shear. In a first series of models, the upper crust was homogeneous and consisted of a single
527 analogue material, either weak microbeads or strong quartz sand. In three further series of models, the upper
528 crust is laterally heterogeneous and consisted of three domains with vertical boundaries and contrasting
529 strength (i.e. a weak-strong-weak or a strong-weak-strong configuration).

530 - The fault pattern in a homogeneous upper crust is dominated by sinistral (synthetic) strike-slip faulting,
531 whose orientations are readily explained by the Mohr-Coulomb failure criterion, with fault strikes
532 being a function of the internal friction angles. In models with heterogeneous upper crust, the
533 development of the faults does not follow an *en echelon* pattern. The sinistral faults are developed in
534 the outer domains, in the expected orientations according to the Mohr-Coulomb failure criterion.

535 - The heterogeneity of the upper crust, as lateral variations of the lithology, could affect the expected
536 sequence of strike-slip faults with antithetic faults being the first to form. If the initial strike of the
537 boundaries of the domains is subparallel to the predicted Mohr-Coulomb, the development of antithetic
538 faults is promoted. As a consequence, faulting may occur in distinct structural domains and faults may
539 be segmented. If the orientation is less favorable, the development of antithetic faults is not promoted,
540 allowing synthetic faults to form without distinct structural domains.

541 - The properties of the lithology that intersect the sinistral faults, influences how their segments are
542 connected. In the case of weak-strong-weak, the synthetic faults from the outer domains cross-cut the
543 central domain with a slight change in strike orientation, whereas in the case of strong-weak-strong,
544 the weak central domain show internal oblique-slip reverse faulting, which inhibits faults from the
545 outer domain to fully cross the central domain.

546 - Although we only tested sinistral simple shear, our results can also be applied to dextral simple shear
547 by mirroring the fault patterns around a N-S axis.

548 - There are similarities between the behaviour of individual faults in natural systems and our
549 heterogeneous upper crustal models, i.e. the slight change in strike orientation when crossing a
550 boundary with contrasting strength.

551

552 **6. Competing interests**

553 The contact author has declared that none of the authors has any competing interests.

554 **7. Acknowledgments**

555 The following work has been partially funded by a predoctoral contract (PREDOC20-073), by the
556 Universidad Rey Juan Carlos and project PID2022-139527OB-I00 funded by
557 MCIN/AEI/10.13039/501100011033/ and FEDER (Ministerio de Ciencia e Innovación; Gobierno de
558 España).

559

560 **8. References**

- 561 Alonso, J. L., Pulgar, J. A., García-Ramos, J. C., & Barba, P.: Tertiary basins and Alpine tectonics in the
562 Cantabrian Mountains (NW Spain). in *Tertiary Basins of Spain* (pp. 214–227). Cambridge
563 University Press, 1996
- 564 Aki, K.: Geometric features of a fault zone related to the nucleation and termination of an earthquake
565 rupture, in: *Proceedings of Conference XLV Fault Segmentation and Controls of Rupture Initiation
566 and Termination*. US Geological Survey Open File Report 89-315, pp. 1–9, 1989
- 567 Anderson, E. M: *The Dynamics of faulting and Dyke Formation with Applications to Britain* (2nd edition),
568 Oliver and Boyd, Edinburgh, Scotland, 1951.
- 569 Antonellini, M.A., Aydin, A., Pollard, D.D.: Microstructure of deformation bands in porous sandstones at
570 Arches National Park, Utah. *J. Struct. Geol.*, 16, 941e959, 1994.
- 571 Aydin, A., Nur, A.: Evolution of pull-apart basins and their scale independence. *Tectonics* 1, 91–105, 1982.
- 572 Aydin, A.: Fractures, faults, and hydrocarbon entrapment, migration and flow. *Mar. Pet. Geol.*, 17, 797–
573 814, 2000.
- 574 Aydin, A., & Berryman, J. G: Analysis of the growth of strike-slip faults using effective medium theory. *J.*
575 *Struct. Geol.*, 32(11), 1629–1642. <https://doi.org/10.1016/j.jsg.2009.11.007>, 2010.
- 576 Barka, A., Kadinsky-Cade, K.: Strike-slip fault geometry in Turkey and its influence on earthquake activity.
577 *Tectonics*, 7, 663–684, 1988.
- 578 Bartlett, W.L., Friedman, M., Logan, J.M: Experimental folding and faulting of rocks under confining
579 pressure Part IX. Wrench faults in limestone layers. *Tectonophysics*, 79, 255–277.
580 [https://doi.org/10.1016/0040-1951\(81\)90116-5](https://doi.org/10.1016/0040-1951(81)90116-5), 1988.

581 Bullock, R. J., De Paola, N., Holdsworth, R. E., & Trabucho-Alexandre, J.: Lithological controls on the
582 deformation mechanisms operating within carbonate-hosted faults during the seismic cycle. *J.*
583 *Struct. Geol.*, 58, 22–42. <https://doi.org/10.1016/j.jsg.2013.10.008>, 2014.

584 Burgmann, R., Pollard, D.D.: Strain accommodation about strike-slip fault discontinuities in granitic rock
585 under brittle-to-ductile conditions. *J. Struct. Geol.*, 16, 1655–1674, 1994.

586 Byerlee, J.: Friction of rocks, pages 615–626. Springer, 1978.

587 Cazarin, C.L., van der Velde, R., Santos, R.V., Reijmer, J.J.G., Bezerra, F.H.R., Bertotti, G., La Bruna, V.,
588 Silva, D.C.C., de Castro, D.L., Srivastava, N.K., Barbosa, P. F.: Hydrothermal activity along a
589 strike-slip fault zone and host units in the São Francisco Craton, Brazil – implications for fluid
590 flow in sedimentary basins. *Precambrian Res.* 365
591 <https://doi.org/10.1016/j.precamres.2021.106365>, 2021.

592 Cheng, X., Ding, W., Pan, L., Zou, Y., Li, Y., Yin, Y., & Ding, S.: Geometry and kinematics characteristics
593 of strike-slip fault zone in complex structure area: A case study from the south no. 15 strike-slip
594 fault zone in the Eastern Sichuan Basin, China. *Front. Earth Sci.*, 10.
595 <https://doi.org/10.3389/feart.2022.922664>, 2022.

596 Cooke, M. L., Toeneboehn, K., and Hatch, J. L.: Onset of slip partitioning under oblique
597 convergence within scaled physical experiments, *Geosphere*, 16, 875–889.
598 <https://doi.org/10.1130/GES02179.1>, 2020.

599 de Joussineau, G., & Aydin, A.: Segmentation along strike-slip faults revisited. *Pure and Applied*
600 *Geophys.* 166(10–11), 1575–1594. <https://doi.org/10.1007/s00024-009-0511-4>, 2009.

601 DeDontney, N., Rice, J. R., & Dmowska, R.: Influence of material contrast on fault branching behavior:
602 BIMATERIAL BRANCHING. *Geophys. Res. Lett.*, 38(14).
603 <https://doi.org/10.1029/2011gl047849>, 2011.

604 Deng, Q., Wu, D., Zhang, P., & Chen, S.: Structure and deformational character of strike-slip fault zones.
605 *Pure and Applied Geophysics*, 124(1–2), 203–223. <https://doi.org/10.1007/bf00875726>, 1986.

606 Dooley, T. P., & Schreurs, G. : Analogue modelling of intraplate strike-slip tectonics: A review and new
607 experimental results. *Tectonophysics*, 574–575, 1–71.
608 <https://doi.org/10.1016/j.tecto.2012.05.030>, 2012

609 Du, Y., & Aydin, A.: Shear fracture patterns and connectivity at geometric complexities along strike-slip
610 faults. *J. Geophys. Res.*, 100(B9), 18093–18102. <https://doi.org/10.1029/95jb01574>, 1995.

611 Fernández, M., Marzán, I., & Torne, M.: Lithospheric transition from the Variscan Iberian Massif to the
612 Jurassic oceanic crust of the Central Atlantic. *Tectonophysics*, 386(1–2), 97–115.
613 <https://doi.org/10.1016/j.tecto.2004.05.005>. 2004

614 Gabrielsen, R. H., Giannenas, P. A., Sokoutis, D., Willingshofer, E., Hassaan, M., & Faleide, J. I.:
615 Analogue experiments on releasing and restraining bends and their application to the study of the
616 Barents Shear Margin. *Solid Earth*, 14(9), 961–983. <https://doi.org/10.5194/se-14-961-2023>,
617 2023

618 Gamond, J.F.: Displacement features associated with fault zones: a comparison between observed examples
619 and experimental models. *J. Struct. Geol.*, 5, 33–45, 1983.

620 Gapais, D., Fiquet, G., & Cobbold, P. R.: Slip system domains, 3. New insights in fault kinematics from
621 plane-strain sandbox experiments. *Tectonophysics*, 188(1–2), 143–157.
622 [https://doi.org/10.1016/0040-1951\(91\)90320-r](https://doi.org/10.1016/0040-1951(91)90320-r), 1991.

623 Gomes, A. S., Rosas, F. M., Duarte, J. C., Schellart, W. P., Almeida, J., Tomás, R., & Strak, V.: Analogue
624 modelling of brittle shear zone propagation across upper crustal morpho-rheological
625 heterogeneities. *J. Struct. Geol.*, 126, 175–197. <https://doi.org/10.1016/j.jsg.2019.06.004>,
626 2019.

627 Harris, R.A., Day, S.M.: Dynamic 3D simulation of earthquakes on en echelon faults. *Geophys. Res. Lett.*,
628 26, 2089–2092, 1999.

629 Hatem, A. E., Cooke, M. L., & Toeneboehn, K.: Strain localization and evolving kinematic efficiency of
630 initiating strike-slip faults within wet kaolin experiments. *J. Struct. Geol.*, 101, 96–108.
631 <https://doi.org/10.1016/j.jsg.2017.06.011>, 2017.

632 Hatem, A. E., Cooke, M. L., & Toeneboehn, K.: Strain localization and evolving kinematic efficiency of
633 initiating strike-slip faults within wet kaolin experiments. *J. Struct. Geol.*, 101, 96–108.
634 <https://doi.org/10.1016/j.jsg.2017.06.011>, 2017.

635 Kim, Y., Peacock, D.C.P., Sanderson, D.J.: Fault damage zones. *J. Struct. Geol.*, 26, 503–517, 2004.

636 Kirkland, C. L., Alsop, G. I., & Prave, A. R.: The brittle evolution of a major strike-slip fault associated
637 with granite emplacement: a case study of the Leannan Fault, NW Ireland. *J. Geol. Soc.*, 165(1),
638 341–352. <https://doi.org/10.1144/0016-76492007-064>, 2008.

639 Lefevre, M., Souloumiac, P., Cubas, N., & Klinger, Y. : Experimental evidence for crustal control over
640 seismic fault segmentation. *Geology*, 48(8), 844–848. <https://doi.org/10.1130/g47115.1>, 2020.

641 Mair, K., Frye, K.M., Marone, C.: Influence of grain characteristics on the friction of granular shear zones.
642 *J. Geophys. Res.*, 107 (B10), 4/1-4/9, 2002.

643 Martel, S.J., Peterson Jr., J.E.: Interdisciplinary characterization of fracture systems at the US/BK site,
644 Grimsel Laboratory, Switzerland. *International Journal of Rock Mechanics and Mining Science and*
645 *Geomechanical Abstracts* 28, 259–323, 1991.

646 Martínez Catalán, J. R., Arenas, R., Díaz García, F., & Abati, J.: Variscan accretionary complex of
647 northwest Iberia: Terrane correlation and succession of tectonothermal events. *Geology*, 25(12),
648 1103. [https://doi.org/10.1130/0091-7613\(1997\)025<1103:vaconi>2.3.co;2](https://doi.org/10.1130/0091-7613(1997)025<1103:vaconi>2.3.co;2). 1997

649

650 Martínez Catalán, J.R. : The Central Iberian arc, an orocline centered in the Iberian Massif and some
651 implications for the Variscan belt. *Int. J. Earth Sci.* 101, 1299–1314.
652 <https://doi.org/10.1007/s00531-011-0715-6>, 2012.

653 Martín-González, F., Heredia, N.: Geometry, structures and evolution of the western termination of the
654 Alpine-Pyrenean Orogen reliefs (NW Iberian Peninsula). *J. Iber. Geol.* 37, 103–120.
655 https://doi.org/10.5209/rev_JIGE.2011.v37.n2.1, 2011.

656 Martín-González, F., Barbero, L., Capote, R., Heredia, N., & Gallastegui, G.: Interaction of two successive
657 Alpine deformation fronts: constraints from low-temperature thermochronology and structural
658 mapping (NW Iberian Peninsula). *Int. J. Earth. Sci.*, 101(5), 1331–1342.
659 <https://doi.org/10.1007/s00531-011-0712-9>. 2012.

660 Matte, P.: Accretionary history and crustal evolution of the Variscan belt in Western
661 Europe. *Tectonophysics*, 196(3–4), 309–337. [https://doi.org/10.1016/0040-1951\(91\)90328-](https://doi.org/10.1016/0040-1951(91)90328-)
662 *p*, 1991.

663 Misra, S., Mandal, N., Chakraborty, C: Formation of Riedel shear fractures in granular materials: Findings
664 from analogue shear experiments and theoretical analyses. *Tectonophysics* 471, 253–259.
665 <https://doi.org/10.1016/j.tecto.2009.02.017>. 2009

666 Moore, J. D. P., & Parsons, B.: Scaling of viscous shear zones with depth-dependent viscosity and power-
667 law stress–strain-rate dependence. *Geophys. J. Int.*, 202(1), 242–260.
668 <https://doi.org/10.1093/gji/ggv143>, 2015.

669 Myers, R., Aydin, A.: The evolution of faults formed by shearing across joint zones in sandstone. *J. Struct.*
670 *Geol.*, 26, 947–966, 2004.

671 Nicholson, C., Seeber, L., Williams, P. and Sykes, L.R.: Seismic evidence for conjugate slip and block
672 rotation within the San Andreas fault system, Southern California. *Tectonics*, 5: 629–648, 1986

673 Odling, N.E., Harris, S.D., Knipe, R.J.: Permeability scaling properties of fault damage zones in siliclastic
674 rocks. *J. Struct. Geol.*, 26, 1727–1747, 2004.

675 Panien, M., Schreurs, G., & Pfiffner, A.: Mechanical behaviour of granular materials used in analogue
676 modelling: insights from grain characterisation, ring-shear tests and analogue experiments. *J. Struct.*
677 *Geol.*, 28(9), 1710–1724. <https://doi.org/10.1016/j.jsg.2006.05.004>, 2006.

678 Peacock, D.C.P., Sanderson, D.J.: Displacement, segment linkage and relay ramps in normal fault zones.
679 *J. Struct. Geol.*, 13, 721–733, 1991.

680 Peacock, D. C. P., & Sanderson, D. J.: Effects of layering and anisotropy on fault geometry. *J. Geol. Soc.*,
681 149(5), 793–802. <https://doi.org/10.1144/gsjgs.149.5.0793>, 1992.

682 Petersen, M. D., Dawson, T. E., Chen, R., Cao, T., Wills, C. J., Schwartz, D. P., & Frankel, A. D.: Fault
683 displacement hazard for strike-slip faults. *BSSA.*, 805–825.
684 <https://doi.org/10.1785/0120100035>, 2011.

685 Preuss, S., Herrendörfer, R., Gerya, T., Ampuero, J.-P., & Dinther, Y.: Seismic and aseismic fault growth
686 lead to different fault orientations. *J. Geophys. Res. Solid Earth.*, 124(8), 8867–8889.
687 <https://doi.org/10.1029/2019jb017324>, 2019.

688 Ramberg, H.: Gravity, deformation and the Earth's crust: In theory, experiments and geological application
689 (p. 452). Academic Press, 1981.

690 Richard, P.: Experiments on faulting in a two-layered cover sequence overlying a reactivated basement
691 fault with oblique-slip. *J. Struct. Geol.* 13, 459–469, 1991.

692 Richard, P., Naylor, M.A., Koopman, A.: Experimental models of strike-slip tectonics. *Pet. Geosci.*, 1, 71–
693 80, 1995.

694 Riedel, W.: Zur Mechanik geologischer Brucherscheinungen. *Centralblatt*. 1929.

695 Rispoli, R.: Stress fields about strike-slip faults inferred from stylolites and tension gashes. *Tectonophysics*
696 75, 729–736, 1981.

697 Ron, H., Freund, R., Garfunkel, Z. and Nur, A.: Block rotation by strike slip faulting: structural and
698 paleomagnetic evidence. *J. Geophys. Res.*, 89: 6256-6270, 1984.

699 Sammis, C. G., G. King, and R. Biegel, The kinematics of gouge deformation, *Pure Appl. Geophys.*, 125,
700 777 – 812, 1987.

701 Schmid, T., Schreurs, G. Warsitzka, M., & Rosenau, M.: Effect of sieving height on density and friction of
702 brittle analogue material: Ring-shear test data of quartz sand used for analogue experiments in the
703 Tectonic Modelling Lab of the University of Bern. GFZ Data Services.
704 <https://doi.org/10.5880/fdgeo.2020.006>, 2020.

705 Scholz, C. H.: *The Mechanics of Earthquakes and Faulting*. Cambridge University Press, 2002.

706 Schreurs, G.: Experiments on strike-slip faulting and block rotation. *Geology*, 22(6), 567.
707 [https://doi.org/10.1130/0091-7613\(1994\)022<0567:eossfa>2.3.co;2](https://doi.org/10.1130/0091-7613(1994)022<0567:eossfa>2.3.co;2), 1994.

708 Schreurs, G.: Structural analysis of the Schams nappes and adjacent tectonic units in the Penninic zone
709 (Grisons, SE-Switzerland). ETH Zurich, 1991.

710 Schreurs, G.: Fault development and interaction in distributed strike-slip shear zones: an experimental
711 approach. In: Storti, F., Holdsworth, R.E., Salvini, F. (Eds.), *Intraplate Strike-slip Deformation*
712 *Belts. Geol. Soc. Spec. Publ.*, 210, 35–52, 2003

713 Shaw, B.E., Dieterich, J.H.: Probabilities for jumping fault segment stepovers. *Geophys. Res. Lett.*, 34,
714 L01307. doi:10.1029/2006GL027980, 2007.

715 Sibson, R.H.: Stopping of earthquake ruptures at dilational fault jogs. *Nature* 316, 248–251, 1985.

716 Stirling, M.W., Wesnousky, S.G., Shimazaki, K.: Fault trace complexity, cumulative slip, and the shape of
717 the magnitude-frequency distribution for strike-slip faults: a global survey. *Geophys. J. Int.*, 124,
718 833–868, 1996.

719 Sylvester, A.G.: Strike-slip faults. *Geol. Soc. Am. Bull.* 100, 1666–1703. [https://doi.org/10.1130/0016-](https://doi.org/10.1130/0016-7606(1988)1002.3.CO;2)
720 [7606\(1988\)1002.3.CO;2](https://doi.org/10.1130/0016-7606(1988)1002.3.CO;2), 1988.

721 Vegas, R., Vicente Muñoz, G., Muñoz Martín, A., & Palomino, R.: Los corredores de fallas de Régua-
722 Verin y Vilarica: Zonas de transferencia de la deformación intraplaca en la Península Ibérica. 2004

723 Veludo, I., Dias, N. A., Fonseca, P. E., Matias, L., Carrilho, F., Haberland, C., & Villaseñor, A.: Crustal
724 seismic structure beneath Portugal and southern Galicia (Western Iberia) and the role of Variscan
725 inheritance. *Tectonophysics*, 717, 645–664. <https://doi.org/10.1016/j.tecto.2017.08.018>.
726 2017

727 Venâncio, M. B., & da Silva, F. C. A.: Structures evolution along strike-slip fault zones: The role of
728 rheology revealed by PIV analysis of analog modeling. *Tectonophysics*, 229764, 229764.
729 <https://doi.org/10.1016/j.tecto.2023.229764>, 2023.

730 Vergés, J., Kullberg, J. C., Casas-Sainz, A., de Vicente, G., Duarte, L. V., Fernández, M., Gómez, J. J.,
731 Gómez-Pugnaire, M. T., Jabaloy Sánchez, A., López-Gómez, J., Macchiavelli, C., Martín-Algarra,
732 A., Martín-Chivelet, J., Muñoz, J. A., Quesada, C., Terrinha, P., Torné, M., & Vegas, R.: An
733 introduction to the alpine cycle in Iberia. En *The Geology of Iberia: A Geodynamic Approach* (pp.
734 1–14). Springer International Publishing. 2019

735 Visage, S., Souloumiac, P., Cubas, N., Maillot, B., Antoine, S., Delorme, A., & Klinger, Y.: Evolution of
736 the off-fault deformation of strike-slip faults in a sand-box
737 experiment. *Tectonophysics*, 847(229704), 229704.
738 <https://doi.org/10.1016/j.tecto.2023.229704>, 2023.

739 Wesnousky, S.G.: Seismological and structural evolution of strike-slip faults. *Nature* 335, 340–342, 1988.

740 Wesnousky, S.G.: Predicting the endpoints of earthquake ruptures. *Nature* 444, 358–360, 2006.

741 Westerweel, J., Scarano, F.: Universal outlier detection for PIV data. *Experiments in fluids* 39,
742 1096-1100, 2005.

743 Zhang, X., & Sagiya, T.: Shear strain concentration mechanism in the lower crust below an intraplate strike-
744 slip fault based on rheological laws of rocks. *EPSL*, 69(1). [https://doi.org/10.1186/s40623-017-](https://doi.org/10.1186/s40623-017-0668-5)
745 [0668-5](https://doi.org/10.1186/s40623-017-0668-5), 2017.

746 Zwaan, F., Schreurs, G., Ritter, M., Santimano, T., & Rosenau, M.: Rheology of PDMS-corundum sand
747 mixtures from the Tectonic Modelling Lab of the University of Bern (CH). V. 1. GFZ data Services.
748 <https://doi.org/10.5880/fdgeo.2018.023>, 2018.